8-16-4 graphyne: Square-lattice two-dimensional nodal line semimetal with a nontrivial topological Zak index

Arka Bandyopadhyay [1], Arnab Majumdar [2,*], Suman Chowdhury [3], Rajeev Ahuja [2,4,†] and Debnarayan Jana [1,‡]

[1]*Department of Physics, University of Calcutta, 92 A P C Road, Kolkata 700009, India*
[2]*Department of Physics and Astronomy, Box 516, Uppsala University, Uppsala, SE-75120, Sweden*
[3]*Skolkovo Institute of Science and Technology, Skolkovo Innovation Center, 3 Nobel Street, Moscow 121205, Russia*
[4]*Department of Materials Science and Engineering, Royal Institute of Technology, Stockholm, SE-10044, Sweden*

(Received 25 August 2020; revised 2 February 2021; accepted 3 February 2021; published 22 February 2021)

An unprecedented graphyne allotrope with square symmetry and nodal line semimetallic behavior has been proposed in the two-dimensional (2D) realm. The emergence of the Dirac loop around the high-symmetry points in the presence of both the inversion and time-reversal symmetries is a predominant feature of the electronic band structure of this system. Besides, the structural stability in terms of the dynamic, thermal, and mechanical properties has been critically established for the system. Following the *exact analytical* model based on the real-space renormalization group scheme and tight-binding approach, we have inferred that the family of 2D nodal line semimetals with square symmetry can be reduced to a universal four-level system in the low-energy limit. This renormalized lattice indeed explains the underlying mechanism responsible for the fascinating emergence of 2D square nodal line semimetals. Besides, the analytical form of the generic dispersion relation of these systems is well supported by our density-functional theory results. Finally, the nontrivial topological properties have been explored for the predicted system without breaking the inversion and time-reversal symmetry of the lattice. We have obtained that the edge states are protected by the nonvanishing topological index, i.e., Zak phase.

DOI: 10.1103/PhysRevB.103.075137

I. INTRODUCTION

The rise of Dirac materials, i.e., graphene [1], topological insulators [2], d-wave superconductors [3], etc. is undoubtedly an important aspect of fundamental science because of their unusual, unique, and robust physical properties [4–6]. In principle, the electronic behavior of any system strongly relies on the corresponding lattice symmetry and dimensionality [7]. With respect to the lattices, the von Neumann–Wigner theorem [8] ascribes a number of constrains that makes the emergence of two-dimensional (2D) Dirac materials rare. Initially, it was perceived that the Dirac fermions are the consequence of graphene's honeycomb crystal and is robust to small external perturbations [9,10]. Likewise, the electronic band structures of graphene analogous silicene and germanene [11,12] also evince the existence of Dirac cone features. But, this curiosity was not bound only to group 4 elements and was extended to numerous 2D allotropes of different elements, such as boron [13], aluminum, phosphorus, nitrogen [14], and so on. Nevertheless, Malko *et al.* [15] revealed that carbon systems with distinct symmetry, α-, β-, and 6,6,12-graphynes also exhibit graphenelike Dirac cones. Among these lattices, 6,6,12-graphyne with rectangular unit cell [15] indicates that the hexagonal symmetry is not a prerequisite for the survival of Dirac fermions. Of late, some additional graphene allotropes, *viz.,* pha- [16], SW- [17], *S*-, *D*-, *E*- [18], PAI-graphene [19], OPG-Z [20], δ- [21], $H_{4,4,4}$− [22], circumcoro-graphynes [23], etc. also join the exotic family of 2D Dirac materials. It is to be noted that the above-mentioned systems belong to either hexagonal or rectangular symmetry groups and can be spontaneously transformed into graphenelike honeycomb lattices [18,24,25].

However, conventional Dirac fermions are particularly hard to find in square lattice [26–29]. In this regard, Zhang *et al.* [30] first explored the coexistence of square symmetry and Dirac fermions by introducing two square graphynes (S graphynes), i.e., 4,12,2- and 4,12,4-graphynes. However, the nearest-neighbor interaction in the above-mentioned systems only allows the formation nodal rings [31] at the crossing points of the valence-band maximum (VBM) and conduction-band minimum (CBM). Besides, Jiang *et al.* [32,33] have recently explored that square Lieb and kagome lattices also possess Dirac fermions. Emergence of the nodal rings also exhibits twofold band degeneracies that disperse linearly along the high-symmetry k path of the irreducible Brillouin zone (IBZ). It is worth mentioning that similar types of nodal rings are further observed for two square lattices namely of tetragonal silicene (T silicene) [34] and tetragonal germanene (T germanene) [35].

The topological phases of material are characterized by some topological invariants. In particular, Chern numbers in 2D Chern insulators [36], $\mathbb{Z}_2$ indices in 2D and 3D topological insulators [37], winding numbers in topological nodal line semimetals [38,39], and topological charges in Weyl semimetals [40] are some well-known symmetry-protected topological

*arnab.majumdar@physics.uu.se
†rajeev.ahuja@physics.uu.se
‡djphy@caluniv.ac.in

invariants. The family of topological insulators involves heavy elements in order to enhance the effect of spin orbit coupling (SOC) [41]. Of late, identification of topological semimetals (TSMs) with stable linear band dispersion near the Fermi level has drawn great interest owing to their fascinating edge or surface states. In this regard, materials made of light elements without SOC effect, i.e., carbon, boron, etc. are highly anticipated to be a promising alternative for future practical applications regarding TSMs [38,39,42].

The real-space renormalization group (RSRG) scheme [43] is a real-space rescaling method to explore the spectral properties of tight-binding Hamiltonians. In particular, in this method, the preferred subset of atomic sites of the original lattice is decimated out to achieve a scaled version of it. The scaled lattice, however, carries all the information of the original lattice in terms of modified hopping parameters. In recent years, to explore the intriguing features of the Dirac states in many square symmetric graphyne system, the RSRG method has been proved to be an extremely useful technique.

In this work, we have explored the underlying rich physics associated with the appearance of these two-dimensional nodal line semimetals and have proposed a square graphyne allotrope with anisotropic nodal points, i.e., 8-16-4 graphyne, where 4 carbon atoms connect neighboring octagons and form 16-membered rings. We will refer to the predicted system by this nomenclature for the rest of the study. The dynamical, mechanical, thermal, and thermodynamic stability of 8-16-4 graphyne have been critically established. Moreover, an exact analytical expression for the generic dispersion relation of not only our predicted systems but the entire class of square symmetric nodal line semimetals (i.e., square nodal lattices) has been obtained. Finally, we have revealed the nontrivial topological aspect of these tetragonal systems with negligible SOC in the presence of both inversion and time-reversal symmetry. Besides, the edge states associated with the quantized Zak phase and the corresponding winding number have also manifested. These results are extremely important in predicting future topological photonics [44,45], acoustic crystals [46,47], etc.

II. METHODOLOGY

The 2D 8-16-4 graphyne structure in this work has been relaxed within the framework of density-functional theory (DFT) [48] by solving the Kohn-Sham equations [49]. The calculations have been carried out by using the projector augmented wave (PAW) [50] method as implemented in the Vienna *Ab initio* Simulation Package (VASP) [51]. A well-converged energy cutoff of 700 eV was used and the Brillouin zone was sampled employing Monkhorst-Pack [52] k-point meshes. $15 \times 15 \times 1$ k-point meshes were employed for all the systems studied. To eliminate the interaction between periodic images, we have maintained a vacuum layer of $\sim$15 Å on either side of the monolayer. The C PAW pseudopotentials were used with the valence states of $2s^2 2p^2$, utilizing the Perdew-Burke-Ernzerhof (PBE) [53] exchange-correlation functional. During the optimization of the atomic positions using the conjugate gradient method, the energy convergence value between two consecutive steps was maintained to be 10^{-6} eV. The force convergence criterion was kept at a value of 0.001 eV/Å. Phonon dispersion curves were calculated by using the density-functional perturbation theory approach in VASP and the q-point interpolation was done using the PHONOPY package [54] by considering a $2 \times 2 \times 1$ supercell. In order to verify thermal stability, we performed *ab initio* molecular dynamics (AIMD) simulation at 1000 K using VASP by considering a $2 \times 2 \times 1$ supercell. Constant volume and constant temperature canonical ensemble was employed with an appropriate Nosé thermostat [55]. The time step used for the integration of the equation of motions was chosen to be 1.0 fs. All MD simulations were performed for 10,000 time steps. Finally, the topological invariants (TI) were determined using the WANNIERTOOLS code [56]. The tight-binding parameters that were used to calculate the TI were obtained from WANNIER90 [57]. The integrated crystal orbital Hamilton population (ICOHP) has been calculated using the LOBSTER code [58] to study the bond strengths. In order to check whether we can predict this 8-16-4 graphyne structure from the evolutionary algorithm, we used USPEX [59–61], which is an extremely powerful tool for predicting thermodynamically stable crystal structures. In this work we have performed fixed-cell (taking the cell parameters as the original graphyne lattice), fixed-composition calculation of the elemental carbon with 16 carbon atoms in the unit cell as the original graphyne allotrope contains 16 atoms in the unit cell. We have generated 40 structures in the first generation. Then 50, 30, and 20% structures are produced by heredity, mutation, and random symmetric structure generator, respectively. In this work the evolutionary searches have been combined with density-functional theory (DFT) [48] within the purview of PBE functional [53] as implemented in the VASP code. We observed that USPEX predicted the desired structure after the first generation with identical lattice parameters as the original structure.

III. RESULTS

A. Structure and stability

At first, we have critically explored the structural properties of the newly predicted structure 8-16-4 graphyne. The ground-state geometry of the system has been depicted in Fig. 1(a). It has been observed that 8-16-4 graphyne is composed of 16 and 2 distinct eight-membered carbon (C) rings. Such tessellation has been chosen on the basis of the following key points. As we essentially want to predict a square lattice, hence the environment along the crystallographic axis $\vec{a}$ and $\vec{b}$ must be identical at the same distance from a fixed point. Besides, in order to avoid the occurrence of half-filled bands giving rise to metallic nature we have considered a bipartite lattice. Here, the nearest-neighbor tight-binding model can be efficiently used to explain the formation of Dirac bands. These Dirac bands near Fermi level are symmetric in nature, which particularly implies the chiral symmetry. It is observed that the eigenstates of energy $-$E directly connected with eigenstates of energy $+E$. This symmetric nature of bands can be characterized by the particle-hole symmetry. This symmetry can be broken by introduction of next-nearest-neighbor hopping terms [41]. In addition, there is no magnetic ordering in the system that essentially protects the time-reversal symmetry.

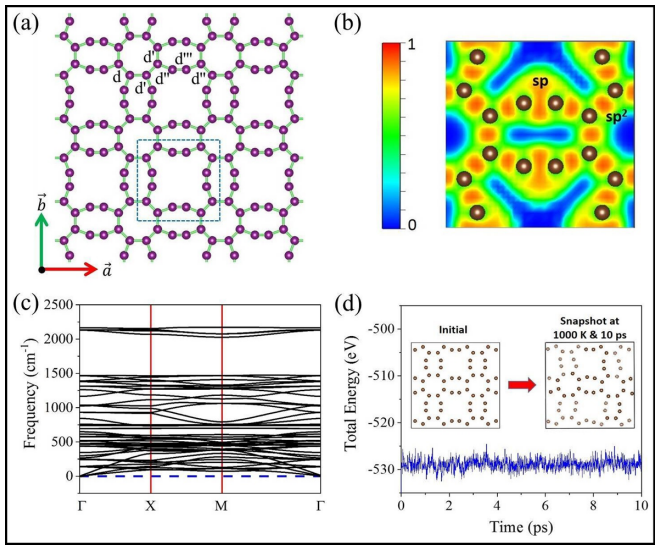

FIG. 1. (a) Ground-state geometry of 8-16-4 graphyne structure. Different types of bonds are indicated. The unit cell has been marked with the blue dotted box. (b) Electron localization function of 8-16-4 graphyne. (c) Phonon dispersion curve of the 8-16-4 graphyne. (d) Total energy vs time of the 8-16-4 graphyne obtained from AIMD simulation at 1000 K. The initial structure at 0 K and a snapshot of the structure at 1000 K after 10 ps of simulation have been shown in the inset.

Precisely, in this system we have adequately incorporated the inversion, mirror reflection, and time-reversal symmetry. Therefore, we strongly expect the symmetry-protected semimetallic behavior of the predicted system. It is clear that the equilibrium lattice of 8-16-4 graphyne belongs to the square symmetry plane group *P*4*mm* with lattice constant 7.35 Å. In particular, the unit cell consists of 16 carbon (C) atoms with different hybridizations. The electron localization function calculation [shown in Fig. 1(b)] reveals that the 16 carbon atoms within the cell are either *sp*- or sp^2 hybridized. This gives rise to four distinct bond lengths labeled in Fig. 1(a) as $d = 1.42$ Å, $d' = 1.48$ Å, $d'' = 1.41$ Å, and $d''' = 1.23$ Å. Indeed, d, d', and d'' are the resonant bonds that correspond to sp^2 hybridization. In contrary, d''' is attributed to the acetylenic linkage between the *sp*-hybridized C atoms. At the Fermi level, the ICOHP values are obtained as −10.26, −10.15, and −10.34 eV per pair corresponding to the bond lengths of d, d', and d'' respectively. As expected, the ICOHP is −15.39 eV per pair for the triple bond. In addition, our predicted system 8-16-4 graphyne has also been obtained using the evolutionary algorithm USPEX [59–61] with the same set of lattice parameters.

In order to establish the plausibility of the existence of this structure, it is imperative to study the dynamical, thermal, and mechanical stabilities of our system along with its formation energy. In Fig. 1(c), the phonon dispersion relation has been depicted and all the modes are positive, therefore the structure is rendered to be dynamically stable. Besides the three acoustic modes, most of the optical modes have frequencies below 1500 cm^{-1} at the Brillouin zone center, but there are four prevalent modes which have much higher frequencies (>2100 cm^{-1}). These four high-frequency optical modes can be attributed to the strong triple bonds and the stretching vibrations between the C atoms with bond length d''' that harden the phonons. This is consistent with other allotropes of graphyne [62]. The transverse acoustic and longitudinal acoustic branches are linear near the Brillouin-zone center, while the out of plane acoustic (*ZA*) branch shows a quadratic nature without a linear component. This is due to the fact that the vertical components along the z direction of the harmonic force constants are zero, which is also observed in other 2D materials [63,64].

TABLE I. Elastic constants (C_{11}, C_{12}, C_{22}, C_{44}) of 8-16-4 graphyne in N/m.

C_{11}	C_{22}	C_{44}	C_{12}
170.78	170.78	14.56	59.48

The thermal stability has also been verified from AIMD simulations [Fig. 1(d)] performed at 1000 K. The total energy oscillates around a mean value (∼−528.85 eV). The final structure after 10 ps retains the basic initial morphology without breaking down into elemental C or converting into any other high-energy allotrope.

The mechanical stability of 8-16-4 graphyne has been established too. The elastic constants relevant to a 2D square lattice (C_{11}, C_{12}, C_{22}, and C_{44}) have been reported in Table I. The Born criteria for stability for square lattices are $C_{11} > 0$, $C_{44} > 0$, $C_{11} > |C_{12}|$, and $(C_{11} + 2C_{12}) > 0$ [65] and they are all satisfied, thus ensuring mechanical stability.

From the elastic constants, the Young modulus (E), Poisson's ratio (υ), in-plane strength (B), shear modulus (G), longitudinal (v_L) and transverse (v_T) velocities, and Debye temperature (θ_D) have also been determined and reported in Table II. The Young modulus (170.78 N/m) and shear modulus (55.65 N/m) obtained are lower compared to that of graphene (345 and 125.40 N/m) [66,67]. It is well expected because of the presence of acetylenic linkages in the system [68].

The thermodynamic stability is determined by calculating the formation energy (E_f) of the system, using the following formula:

$$E_f = \frac{[E_{\text{Total}} - n_C E_C]}{n_C}, \tag{1}$$

where E_{Total}, E_C, and n_C are the total energy of the system, energy of a single carbon atom, and the number of carbon atoms in the unit cell, respectively. The formation energy of the 8-16-4 graphyne allotrope is −8.32 eV/atom, which is comparable to that of the other predicted allotropes [69,70]. In fact, our system is slightly more stable than successfully fabricated α-graphyne [71–73] as well.

TABLE II. Young's modulus (E), Poisson's ratio (υ), in-plane stiffness (B), shear modulus (G), longitudinal (v_L) and transverse (v_T) velocities, and Debye temperature (θ_D) of 8-16-4 graphyne.

E (N/m)	υ	B (N/m)	G (N/m)	v_L (km/s)	v_T (km/s)	θ_D (K)
150.06	0.35	115.13	55.65	17.00	13.96	2170.75

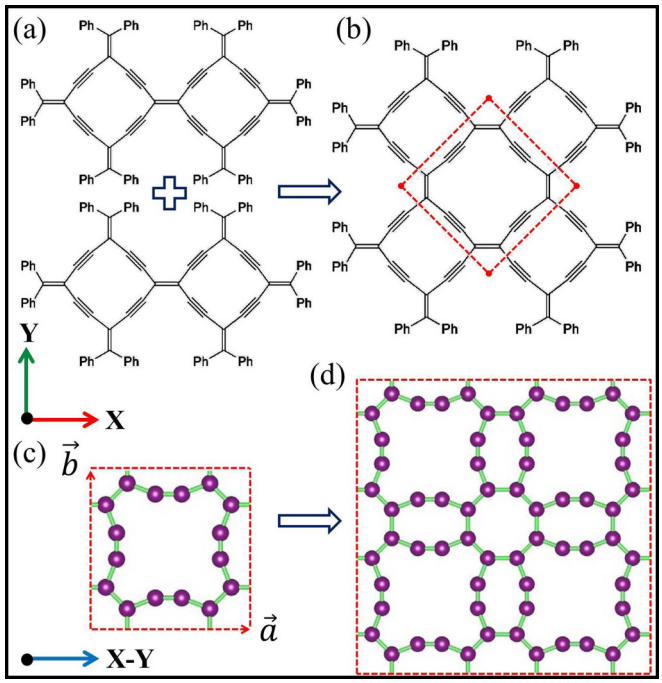

FIG. 2. One of the proposed possible chemical ways to realize the substructure or building block of the system 8-16-4 graphyne. (a) Two expanded bisradialenes are connected sidewise. Ph represents the pendent phenyl groups. (b) The section inside the box resembles the unit cell of 8-16-4 graphyne. (c) The unit cell and translation vectors of 8-16-4 graphyne. (d) The 8-16-4 graphyne sheet obtained from the periodic arrangement of the unit cell along the *X*-*Y* axis.

Being motivated by the previous experiments on the graphyne synthesis [74–76], we have additionally sketched a proposed possible chemical route to realize our predicted system in Fig. 2. The highly conjugated carbon-rich system bisexpanded radialene or bisradialene acts as an important ingredient in designing various graphyne oligomers. Here, we have intuitively explored that two expanded bisradialenes can be connected side by side to achieve the desired subsystem of 8-16-4 graphyne. This subsystem serves as a building block of the 2D 8-16-4 graphyne systems. Periodic arrangement of such subsystems along the *X*-*Y* axis will give rise to the 2D sheet as shown in Fig. 2.

B. Electronic properties

The electronic band structure and partial electronic density of states (PDOS) obtained from PBE approximation is shown in Fig. 3. The VBM and CBM of 8-16-4 graphyne meet at two distinct points of the symmetry path of the IBZ, namely between the *X* and *M* points, and the *M* and Γ points. We have considered the smallest possible unit cell to avoid the band-folding effect due to the use of a larger supercell [77]. This gives rise to zero density of states at the Fermi level, which confirms the semimetallic behavior of the system. The near-Fermi energy states are primarily made up of p_z atomic orbitals. As mentioned above, both sp^2- and *sp*-hybridized C atoms are present in graphyne, resulting in several different bond types. The two sp^2 C atoms are bonded by $\sigma+\pi$. While, the σ bond is contributed by p_x, p_y, and *s* orbitals

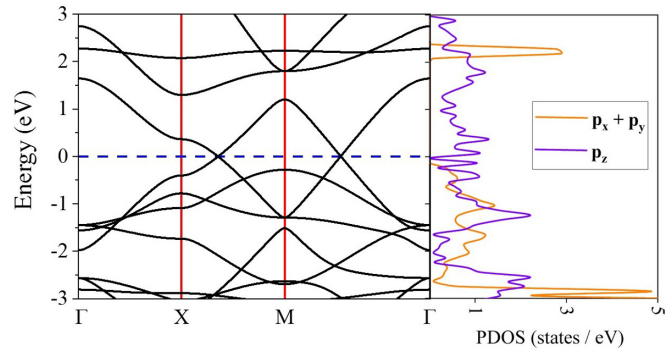

FIG. 3. Electronic band structure and PDOS of 8-16-4 graphyne from PBE approximation.

of C atom, the π bond originates due to the p_z orbital. The two *sp*-hybridized C atoms are bonded by $\sigma + 2\pi$ bonds. In the valence region, there is contribution from all the three *p* orbitals barring in the vicinity of the Fermi level, but in the conduction band, the major contribution is from the p_z orbitals. Furthermore, we have compared our band structure with the previously reported nodal line semimetals with square symmetry, *viz*., 4,12,2-graphyne [30], 4,12,4-graphyne [30], T silicene [34], and T germanene [35]. We have observed that the band structures near the Fermi level exhibit similar appearance. In the next section, we have critically addressed this universality of square nodal line semimetals near the Fermi level.

C. Universality of square Dirac materials

Here, we shall explore and adequately explain the emergence of universal band structure of the square nodal line semimetals in 2D. The computed PDOS in Fig. 3 indicates the dominant contribution of p_z orbital in the vicinity of the Fermi level. We have, therefore, proposed an elegant *analytical approach* to transform the system into an equivalent reduced network under the low-energy approximation. Here, the real-space renormalization group (RSRG) scheme [78] has been extensively used to integrate out specific subsets of atomic sites in the light of tight-binding approximation. The detailed justification and mechanism of this method has been outlined in the recent review article [28].

For the case of lattice, Schrödinger's equation can be discretized and written in terms of difference equation as given below:

$$(E - \epsilon_i)\varphi_i = \sum_j t_{ij}\varphi_j. \tag{2}$$

In Eq. (2), E, ϵ_i, t_{ij}, and φ_i are the energy, on-site potential at the *i*th site, hopping integral between *i*th to *j*th site, and probability amplitude at the *i*th site, respectively. Here, the electrons are allowed to jump between the connected neighbors only. Since the band structure is symmetrical in the VB and CB near Fermi level, therefore only nearest-neighbor interaction is considered. We can use this Eq. (2) for various sites of the mother lattice to eliminate preferred subsets of it.

We have started the process by choosing a specific part of the pristine lattice as indicated in Fig. 4. Here, we want to

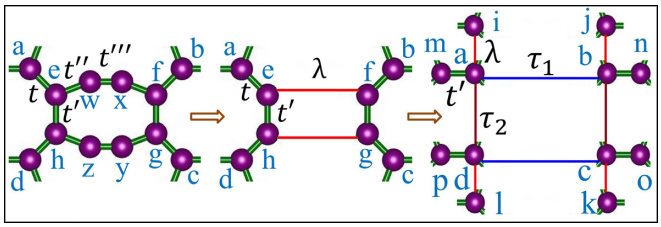

FIG. 4. The RSRG steps for the section of the original lattice. Here, we have first decimated the probability amplitudes of the *w, x, y,* and *z* sites, and then in the second step we have eliminated *e, f, g,* and *h* sites.

decimate the sites forming acetylenic linkages, *viz.*, *w, x, y,* and *z* [29,79]. It is evident that the difference equations can be written using Eq. (2) as follows:

$$\begin{aligned}(E-\epsilon)\varphi_{e(h)} &= t\varphi_{a(d)} + t'\varphi_{h(e)} + t''\varphi_{w(z)},\\ (E-\epsilon)\varphi_{w(z)} &= t''\varphi_{e(h)} + t'''\varphi_{x(y)},\\ (E-\epsilon)\varphi_{x(y)} &= t''\varphi_{f(g)} + t'''\varphi_{w(z)},\\ (E-\epsilon)\varphi_{f(g)} &= t\varphi_{b(c)} + t'\varphi_{g(f)} + t''\varphi_{x(y)}\,. \end{aligned} \tag{3}$$

Here, we have considered uniform on-site potential (ϵ) that equals to E_F and there are four different hopping parameters t, t', t'', and t'''. It is worth mentioning that consideration of uniform on-site energy for sp^2- and sp-hybridized atoms is not perfectly an accurate approximation. However, it has previously been reported for other graphynes, *viz.*, α-, β-, γ-, (6,6,12)-, T graphynes, etc. that this approximation indeed accurately predicts the band dispersion near the Fermi level [28,29,79]. Furthermore, near Fermi level we can approximate $E \approx \epsilon$ and this leads to the following relations:

$$\begin{aligned}\varphi_{w(z)} &= -\tfrac{t''}{t'''}\varphi_{f(g)}\\ \varphi_{x(y)} &= -\tfrac{t''}{t'''}\varphi_{e(h)}.\end{aligned} \tag{4}$$

Substituting the above values into Eq. (3), we obtained the following relations:

$$\begin{aligned}(E-\epsilon)\varphi_{e(h)} &= t\varphi_{a(d)} + t'\varphi_{h(e)} + \lambda\varphi_{f(g)}\\ (E-\epsilon)\varphi_{f(g)} &= t\varphi_{b(c)} + t'\varphi_{g(f)} + \lambda\varphi_{e(h)}.\end{aligned} \tag{5}$$

It is worth mentioning that in the original lattice the electrons hop from site e (h) to f (g) via the triple bond. Nevertheless, the renormalized lattice permits a direct hopping between the above-mentioned sites with the effective hopping parameter, $\lambda = -t''^2/t'''$. The minus sign invariably refers to the fact that the hopping parameter gains an additional phase of $e^{\pm i\pi}$ while passing through the acetylenic linkages. Therefore, this RSRG process has reduced the number of atoms per unit cell from 16 to 8 without altering the physics near Fermi level. Moreover, we aim to continue the decimation process to reduce the degree of difficulty even more.

For that purpose, we have considered a section of the output lattice of the first RSRG process as depicted in Fig. 4. Here, we shall eliminate the *e, f, g,* and *h* sites to achieve direct hopping between *a, b, c,* and *d* using the second RSRG scheme. The key factor of the decimation process remains the same, i.e., $E \approx \epsilon$. Here, in principle (*a, b, c, d*) sites can also be eliminated. However, the structure belongs to the square symmetry group. As a result, the system remains invariant under the transformation $x \to y$ and $y \to x$. In other words, if we rotate the system by 90° it looks identical to the initial lattice as depicted in Fig. S1 of the Supplemental Material [80]. We can see from Fig. S1 that the (*a, b, c, d*) sites of the initial lattice are now (*e, f, g, h*) sites of the rotated system. Therefore, it is clear that these choices are identical because of the fourfold lattice symmetry. This feature has also been reflected in the similar nature of the band structure about the S point, i.e., along the $S(\mathrm{M})\to X$ and $S(M)\to Y(X')$ symmetry path of the Brillouin zone. Γ,X,$S(M)$,$Y(X')$,Γ shown in Fig. S2 of the Supplemental Material [80].

We can write the difference equations for the second RSRG process as follows:

$$\begin{aligned}(E-\epsilon)\varphi_{a(d)} &= t\varphi_{e(h)} + t'\varphi_{m(p)} + \lambda\varphi_{i(l)},\\ (E-\epsilon)\varphi_{b(c)} &= t\varphi_{f(g)} + t'\varphi_{n(o)} + \lambda\varphi_{j(k)},\\ (E-\epsilon)\varphi_{e} &= t\varphi_{a} + t'\varphi_{h} + \lambda\varphi_{f},\\ (E-\epsilon)\varphi_{f} &= t\varphi_{b} + t'\varphi_{g} + \lambda\varphi_{e},\\ (E-\epsilon)\varphi_{g} &= t\varphi_{c} + t'\varphi_{f} + \lambda\varphi_{h},\\ E-\epsilon)\varphi_{h} &= t\varphi_{d} + t'\varphi_{e} + \lambda\varphi_{g}.\end{aligned} \tag{6}$$

We have judiciously simplified Eq. (6) to integrate out *e, f, g,* and *h* sites from the lattice. In particular, we have obtained

$$\left(E-\varepsilon-\frac{t'^2+\lambda^2}{E-\varepsilon}\right)\varphi_e = t\varphi_a + \frac{t\lambda}{E-\varepsilon}\varphi_b + \frac{tt'}{E-\varepsilon}\varphi_d + \frac{2\lambda t'}{E-\varepsilon}\varphi_g \tag{7}$$

and

$$\left(E-\varepsilon-\frac{t'^2+\lambda^2}{E-\varepsilon}\right)\varphi_g = t\varphi_c + \frac{t\lambda}{E-\varepsilon}\varphi_d + \frac{tt'}{E-\varepsilon}\varphi_b + \frac{2\lambda t'}{E-\varepsilon}\varphi_e. \tag{8}$$

As shown in the Appendix, Eq. (7) can be transformed in the following form under the condition $E \approx \epsilon$:

$$\varphi_e = -\frac{t\lambda}{t'^2+\lambda^2}\varphi_b - \frac{tt'}{t'^2+\lambda^2}\varphi_d - \frac{2\lambda t'}{t'^2+\lambda^2}\varphi_g. \tag{9}$$

Similarly, Eq. (8) can also be written as follows:

$$\varphi_g = -\frac{tt'}{t'^2+\lambda^2}\varphi_b - \frac{t\lambda}{t'^2+\lambda^2}\varphi_d - \frac{2\lambda t'}{t'^2+\lambda^2}\varphi_e. \tag{10}$$

Evidently, we can get similar equations for sites f and h, as described below:

$$\varphi_f = -\frac{t\lambda}{t'^2+\lambda^2}\varphi_a - \frac{tt'}{t'^2+\lambda^2}\varphi_c - \frac{2\lambda t'}{t'^2+\lambda^2}\varphi_h, \tag{11}$$

and

$$\varphi_h = -\frac{tt'}{t'^2+\lambda^2}\varphi_a - \frac{t\lambda}{t'^2+\lambda^2}\varphi_c - \frac{2\lambda t'}{t'^2+\lambda^2}\varphi_f. \tag{12}$$

These are two sets of coupled equations that have been further simplified. As a result, the following expressions have

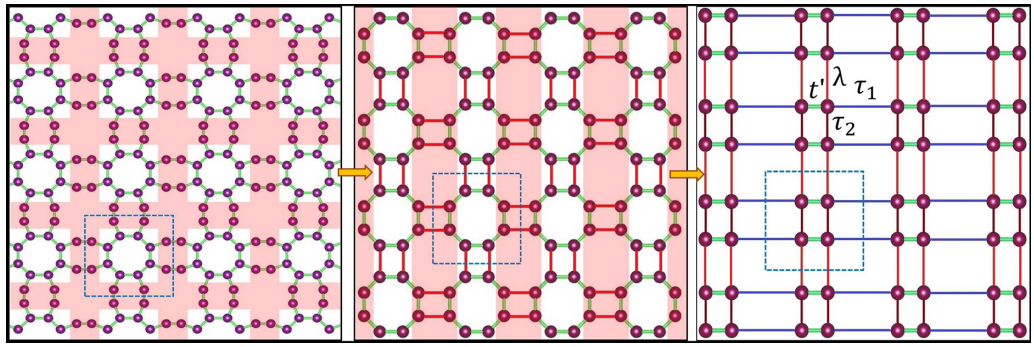

FIG. 5. Effect of the complete RSRG processes on the original lattice of 8-16-4 graphyne. The red shaded sites are decimated to obtain the final lattice. Unit cells of all the lattices are marked with blue dotted boxes.

been obtained:

$$\begin{aligned}
\varphi_e &= \tfrac{t\lambda}{t'^2-\lambda^2}\varphi_b - \tfrac{tt'}{t'^2-\lambda^2}\varphi_d,\\
\varphi_f &= \tfrac{t\lambda}{t'^2-\lambda^2}\varphi_a - \tfrac{tt'}{t'^2-\lambda^2}\varphi_c,\\
\varphi_g &= \tfrac{t\lambda}{t'^2-\lambda^2}\varphi_d - \tfrac{tt'}{t'^2-\lambda^2}\varphi_b,\\
\varphi_h &= \tfrac{t\lambda}{t'^2-\lambda^2}\varphi_c - \tfrac{tt'}{t'^2-\lambda^2}\varphi_a.
\end{aligned} \tag{13}$$

Furthermore, we have cast these values in Eq. (6) and obtained the relations for the renormalized lattice without *e, f, g,* and *h* sites:

$$\begin{aligned}
(E-\varepsilon)\varphi_a &= \tau_1\varphi_b + \tau_2\varphi_d + t'\varphi_m + \lambda\varphi_i,\\
(E-\varepsilon)\varphi_b &= \tau_1\varphi_a + \tau_2\varphi_c + t'\varphi_n + \lambda\varphi_j,\\
(E-\varepsilon)\varphi_c &= \tau_1\varphi_d + \tau_2\varphi_b + t'\varphi_o + \lambda\varphi_k,\\
(E-\varepsilon)\varphi_d &= \tau_1\varphi_c + \tau_2\varphi_a + t'\varphi_p + \lambda\varphi_l
\end{aligned} \tag{14}$$

In the above Eq. (14), τ_1 and τ_2 are the renormalized hopping parameters of the reduced lattice with values $\tau_1 = t^2\lambda/(t'^2-\lambda^2)$ and $\tau_2 = -t^2t'/(t'^2-\lambda^2)$. As an interesting note, the obtained lattice parameters are no longer functions of energy and have real values. In addition, the on-site potential of the low-energy lattice remains the same as the original lattice. Similar to the first RSRG process, we have extended these results to the complete lattice and have depicted it in Fig. 5

The final lattice consists of four atoms per unit cell and is a reasonably simple system to obtain the low-energy dispersion relation analytically. The straightforward method in this regard is to solve the matrix eigenvalue equation of the form $E\varphi = [h(\vec{k})]\varphi$. In this case, the Hamiltonian matrix $[h(\vec{k})]$ can be obtained from the discrete Fourier transform of the lattice because of the translational symmetry and will be (4×4) in dimension, since the number of basis orbitals or sites per unit cell is 4 here. Hence, four eigenvalues of the Hamiltonian matrix will give four branches of the band structure. Among those, we expect two low-energy branches will construct the Dirac nodal points at specific $\vec{k}$ values. In fact, the renormalization process has made this problem way simpler. We can see that there is no cross-hopping integral present in the system. As a direct consequence, we can consider the final lattice as periodic arrangements of chains of dimers along two mutually orthogonal axes. Along one direction (crystallographic $\vec{a}$ axis) the hopping parameters t' and τ_1 are arranged alternatively. On the contrary, the alternative hopping integrals are τ_2 and λ along the perpendicular direction (crystallographic $\vec{b}$ axis). It is well known that a one dimensional (1D) lattice with two atoms per unit cell gives us two branches in the band structure with dispersion relation $\tilde{E} = \epsilon_0 \pm (t_1^2 + t_2^2 + 2t_1t_1\cos qa)^{1/2}$. Here, ϵ_0, t_1, t_2, and a are the on-site potential, alternating hopping parameters, and lattice constant of the chain of dimers, respectively. In our case, the on-site potential is uniform and thus considered to be the zero or reference energy. Hence, two mutually orthogonal 1D chain of dimers will give us two pairs of dispersion relations as follows:

$$\begin{aligned}
E_1 &= \pm\alpha = \pm\left[\tau_1^2 + t'^2 + 2\tau_1 t'\cos(q_y a)\right]^{1/2}\\
E_2 &= \pm\beta = \pm[\tau_2^2 + \lambda^2 + 2\tau_2\lambda\cos(q_x a)]^{1/2}.
\end{aligned} \tag{15}$$

The linear combination of these dispersion relations will provide four branches of the final renormalized lattice. Therefore, the equations of the four branches are $|\alpha+\beta|$, $-|\alpha+\beta|$, $|\alpha-\beta|$, and $-|\alpha-\beta|$. Among these, the last two lie near the E_F and are naturally our point of interest. Considering, $q = (\frac{2\pi k}{a})$, we have expressed the low-energy dispersion in terms of crystal momenta as follows:

$$\begin{aligned}
E_\pm = \pm\Big|&\left[\tau_1^2 + t'^2 + 2\tau_1 t'\cos(2\pi k_y)\right]^{1/2}\\
&-\left[\tau_2^2 + \lambda^2 + 2\tau_2\lambda\cos(2\pi k_x)\right]^{1/2}\Big|.
\end{aligned} \tag{16}$$

In order to justify our exact analytical result, we have simultaneously plotted it with the DFT-based numerical output along the symmetry path $\Gamma(0.0,\ 0.0) \to X(0.0,\ 0.5) \to M(0.5,\ 0.5) \to \Gamma(0.0,\ 0.0)$ in Fig. 6(a). It can be noticed that the dispersion relation given in Eq. (16) reveals the same set of band touching points at (0.19, 0.5) and (0.30, 0.30) as predicted by DFT for the hopping parameters $t = -1.000\ |\tau|$, $t' = -0.890\ |\tau|$, and $\lambda = +0.891\ |\tau|$; here, "$|t| = |\tau| = 2.8$ eV" is the same as the magnitude of graphene's hopping integral [1]. The site-specific band structure of 8-16-4 graphyne, depicted in Fig. S3 of Supplemental Material [80] indicates that formation of Dirac bands near the Fermi level supports the simplified four-level mechanism. The analytical expressions for the coordinates of nodal points are as follows. The nodal points between the symmetry points $X \to M$ and $M \to \Gamma$ lie at $(\tilde{k_x}, 0.5)$ and $(\tilde{k}, \tilde{k})$, respectively. Here, the expressions for $\tilde{k_x}$ and $\tilde{k}$ are

$$\tilde{k_x} = \frac{1}{2\pi}\cos^{-1}\left[1 + \frac{(\tau_1^2 + t'^2) - (\tau_2^2 + \lambda^2)}{2\lambda\tau_2}\right] \tag{17}$$

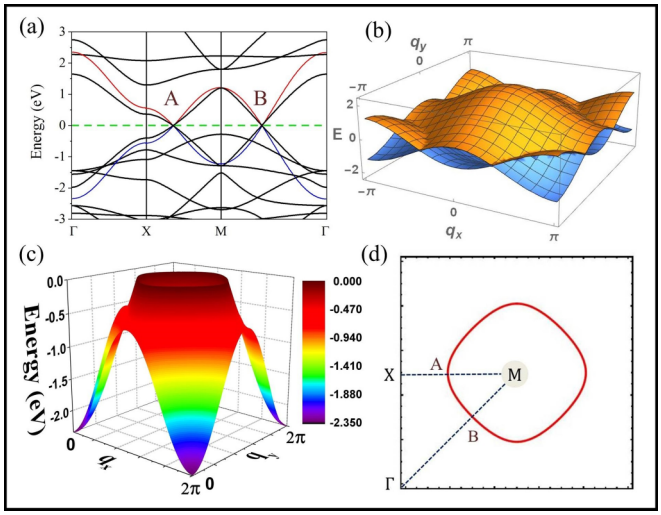

FIG. 6. (a) Analytically obtained band structure of 8-16-4 graphyne is plotted with the our DFT data. Red and blue lines indicate conduction and valence bands, respectively. (b) The 3D plot of the corresponding analytical dispersion relation. Here, E_F is set to zero. (c) Close view of the 3D valence band from analytical expression. Nodal loop around the M point of the BZ is clearly visible. (d) The Dirac nodal loop around the symmetry point M shown by red circle. A and B are two nodal points situated at the symmetry line. Here, lattice constant is considered to be unity.

and

$$\tilde{k} = \frac{1}{2\pi}\cos^{-1}\left[\frac{(\tau_1^2 + t'^2) - (\tau_2^2 + \lambda^2)}{4\lambda\tau_2}\right]. \tag{18}$$

We have already mentioned that the other two parameters τ_1 and τ_2 are not independent but depend on the other hopping integrals. These hopping parameters follow the desirable conditions $|t'| \approx |\lambda|$ and $|\tau_1| \approx |\tau_2|$. Here, we can observe that this analytical approach has spontaneously incorporated small but finite anisotropy in hopping parameters. This in turn restricts the infinite number of contacts between the VB and CB forming flat bands at the Fermi level along the $M \to \Gamma$ path. It is worth mentioning that this nodal point along $M \to \Gamma$ is a unique feature of the square systems and is attributed to the mirror reflection symmetry. In case of rectangular lattices like S graphene, two touching points occur but none of these lie along the $M \to \Gamma$ path [25]. For better understanding, we have plotted the 3D band structure of 8-16-4 graphyne obtained analytically in Figs. 6(b) and 6(c). It is clear from these two figures that VBM and CBM touch each other at the Fermi level and construct Dirac loop, which marks an energy band tangency circle around the symmetry point M. The contour plot of this Dirac nodal ring has been clearly depicted in Fig. 6(d). Here, it is worth mentioning that the band structure obtained from the tight-binding (TB) Hamiltonian written for the mother lattice of 8-16-4 graphyne also exhibits similar behavior near Fermi level (not shown). We have further tuned the phase factor of the renormalized hopping parameter λ (say, $\lambda' = -\lambda/\sqrt{2}$), as, it depends on the number of consecutive triple bonds in the system, and we observed that the corresponding nodal points are located at $\Gamma \to X$ and $M \to \Gamma$ as depicted in Fig. S4 of the Supplemental Material [80]. This elucidates that the nodal point between $M \to \Gamma$ is robust to the alteration of the sign of λ. Besides, the symmetry of the VB and CB is associated with the fact that the C atoms of the unit cell can be divided into two subgroups because of the bipartite nature. The dispersion relation between different symmetry points has been listed in Table S1 of the Supplemental Material [80].

Furthermore, we have calculated the Fermi velocity (v_F) near two distinct nodal points. Therefore, we have expanded the dispersion relations between $X \to M$ and $M \to \Gamma$ in Taylor series about the degenerate points. The quadratic and higher-order terms have been neglected. The linear part has been compared to $E^L = |\hbar v_F \Delta q|$. Here, Δq is equal to $|q - q_0|$, where q_0 is the position of the nodal point and E^L is the energy expansion up to linear order. We have obtained the following expressions of v_F,:

$$v_F|_{X\to M} = \left|\frac{a\tau\tau_2\lambda}{\hbar\beta(k_x)}\sin(2\pi k_x)\right|_{k_x=\tilde{k_x}} = 4.10 \times 10^5\ \text{m/s} = \frac{c}{732} \tag{19}$$

and

$$v_F|_{M\to\Gamma} = \left|\frac{a\tau\tau_2\lambda}{\hbar}\sin(2\pi k)\left(\frac{1}{\alpha(k)} + \frac{1}{\beta(k)}\right)\right|_{k=\tilde{k}} = 8.27 \times 10^5\ \text{m/s} = \frac{c}{363}. \tag{20}$$

Here, c is the speed of light in free space. As mentioned earlier $|\tau| = |t| = 2.8$ eV. Therefore, we can see that $v_F|_{M\to\Gamma}$ is almost twice of $v_F|_{X\to M}$. This indicates highly anisotropic features of the dispersion relation near the two nodal points. Besides, $v_F|_{M\to\Gamma}$ is even slightly higher than the Fermi velocity of graphene as shown in Table S2 of the Supplemental Material [80].

In the above discussions, we have explored that the low-energy lattice of 8-16-4 graphyne judicially explains the emergence of two nodal points either at $\Gamma \to X$ and $M \to \Gamma$ or $X \to M$ and $M \to \Gamma$. With this notion, we have further renormalized the previously predicted 2D square Dirac allotropes (4,12,2 graphyne and 4,12,4 graphyne) and explored that these systems can be invariably cast into the low-energy version of 8-16-4 graphyne as shown in Figs. 7 and 8.

Moreover, a careful observation indicates that the original lattice of T silicene [34] and T germanene [35] resembles the output lattice of 8-16-4 graphyne after the first RSRG process. We can check that the unit cell of all the systems possesses eight atomic sites. However, in this case there is an additional restriction, i.e., $\lambda \approx t_1 \approx t'$. Besides, both the T silicene and T germanene systems possess appreciable spin-orbit coupling that invariably splits the bands. It is worth mentioning that the output of the second RSRG process on T silicene and T germanene is identical to the lattice given in Fig. 3(a). In this case, the renormalized hopping parameters are estimated to be $\tau_1 = t^2\lambda/(t_1^2 - \lambda^2)$ and $\tau_2 = -t^2 t_1/(t_1^2 - \lambda^2)$. Here also the conditions $|t'| \approx |\lambda|$ and $|\tau_1| \approx |\tau_2|$ hold well. These results clearly illustrate that the class of 2D nodal line semimetals

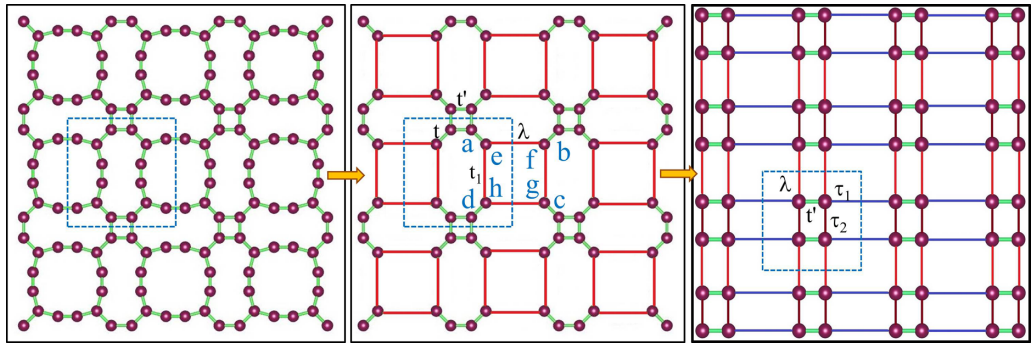

FIG. 7. The decimation process of 4,12,2-graphyne. In the renormalized lattice we have $\boldsymbol{\lambda \approx t_1}$.

with square symmetry follow the universal dispersion relation given in Eq. (16). Indeed, the dispersion relation is attributed to the identical low-energy lattice of the family obtained from the RSRG process. In other words, every square lattice featuring two Dirac nodal points situated at the symmetry line can be renormalized to the same universal network as shown in Figs. 5 , 7, and 8. This efficiently explains the underlying physics behind the fascinating coexistence of square symmetry and Dirac nodal rings.

D. Topological properties

Finally, we have explored the nontrivial topological aspect of both the original and low-energy lattice of 8-16-4 graphyne. As the inversion and time-reversal symmetry are simultaneously present in the systems, the Zak phase ($z = i \oint dq \langle \psi_q^n | \partial \psi_q^n \rangle$) has been calculated via the TB model to serve as a quantized topological index [81]. It is evident that the occurrence of robust topological edge states is a signature of charge polarization and it is intimately related to the topological index, i.e., z or $W = z/\pi$ (winding number) through bulk-edge correspondence. In case of the universal lattice, we initially considered the following conditions $|\tau_1| \approx \lambda \approx |t_{\text{in}}|$ and $|\tau_2| \approx |t'| \approx |t_{\text{out}}|$ and observed a phase transition about $|t_{\text{in}}| = |t_{\text{out}}|$. In particular, $|t_{\text{out}}/t_{\text{in}}| > 1$ gives rise to the topologically nontrivial phase and thus induces robust edge states in the 1D nanoribbon geometry as depicted in Fig. 9(a). The vectored Zak phase in 2D or the wave polarization [82] can be obtained via

$$\vec{P} = \frac{1}{2\pi} \int dk_x dk_y \, Tr[\langle \psi | i \partial_{\vec{k}} | \psi \rangle]. \tag{21}$$

Here, the integration is over the first BZ. In presence of inversion symmetry, $\vec{P}$ can be calculated gauge independently by considering the parities at Γ and X symmetry points:

$$p_i = \frac{1}{2}\left(\sum_n q_i^n \, modulo \, 2\right), \quad (-1)^{q_i^n} \frac{\eta(X_i)}{\eta(\Gamma)}. \tag{22}$$

Here, η represents the parity, i stands for x or y, and the summation is taken over all the occupied bands. In the above-mentioned topologically nontrivial phase, we have obtained $P_x = P_y = 1/2$. This is well expected because of the C_4 symmetry of the bulk system. The above-mentioned polarization forms a $\mathbb{Z}_2$ topological invariant of the system [83]. It is important to note that the conventional $\mathbb{Z}_2$ number as obtained here from product of parities at time-reversal invariant points for time-reversal invariant topological phase is always trivial [82]. Nevertheless, the T-Ge and T-Sn square lattices exhibit nontrivial $\mathbb{Z}_2$ invariant in the presence of strong SOC [35]. As our primary focus is the all-carbon systems and photonic crystals we have characterized the topological phases in terms of Zak phase as mentioned above. A similar type of topological phase transition has previously been predicted in Su-Schrieffer-Heeger lattices and also observed in experiments [82–85]. Furthermore, we proceed to discuss the possibility of the occurrence of the topological edge states in finite ribbon ($N = 2$) with completely distinct hopping parameters i.e., $|\tau_1| \neq |\tau_2| \neq \lambda \neq |t'|$. Here, we define two dimensionless parameters $p_1 = |\tau_1|/|t'|$ and $p_2 = |\lambda|/|\tau_2|$ that essentially determine the phase transition. Consequently, we have calculated the topological invariants for four typical

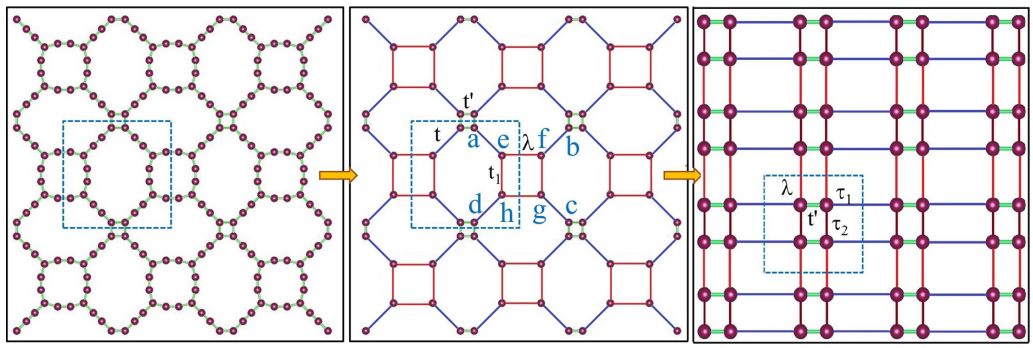

FIG. 8. The decimation process of 4,12,4-graphyne. In the renormalized lattice we have $\boldsymbol{\lambda \approx t_1}$.

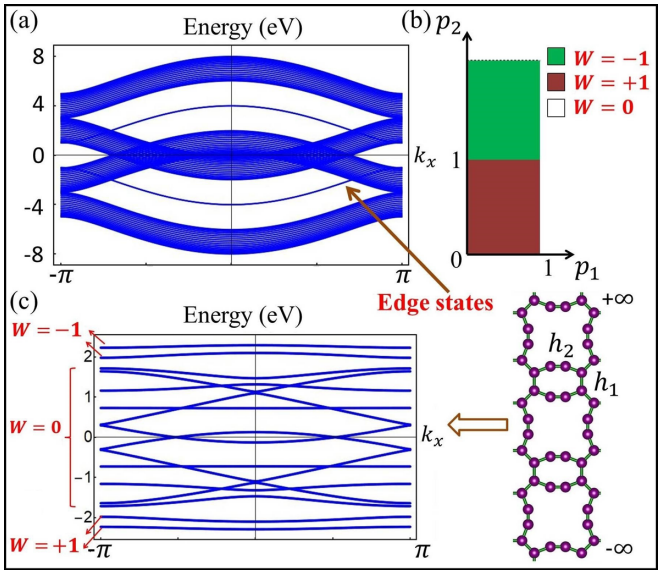

FIG. 9. (a) The topologically nontrivial phase of the low-energy lattice with $|t_{\text{in}}| = 1$ eV and $|t_{\text{out}}| = 2$ eV. The emergence of topologically protected edge state is also shown. Here, we have considered $N = 20$. The edge states are indicated by arrow; the symmetrically opposite bands of the indicated bands in the CB or VB are also edge states. (b) Topological phase diagram of the finite low-energy ribbons with completely distinct hopping parameters. (c) The topological nontrivial phase of 8-16-4 graphyne ribbon ($N = 1$) with $z = +2\pi$ and $W = +2$. Here, we have considered $|h_1| = -1$ eV and $|h_2| = -0.8$ eV.

choices of $p = \binom{p_1}{p_2}$, i.e., $\binom{p_1 > 1}{p_2 > 1}$, $\binom{p_1 > 1}{p_2 < 1}$, $\binom{p_1 < 1}{p_2 > 1}$, and $\binom{p_1 < 1}{p_2 < 1}$. Among these choices, only the last two offer topologically nontrivial phases characterized by $W = +1$ (or, $z = +\pi$) and $W = -1$ (or, $z = -\pi$), respectively. The topological phase diagram in this case has been depicted in Fig. 9(b) and the winding number corresponding to each eigenstate has been presented in Fig. S5 of the Supplemental Material [80]. Finally, we are curious to search for similar nontrivial topological properties for the case of the 8-16-4 graphyne nanoribbon as shown in Fig. 9(c). In this case, the obtained value of z for the real hopping parameters $t = t' = t'' = h_1 = -2.8$ eV and $t''' = h_2 = -3.2$ is $+\pi$ establishing the nontrivial topological feature. Our PBE result also reveals the nontrivial topological phase of the 8-16-4 graphyne sheet (not shown) from WANNIER90 [55,56]. Furthermore, we have explored different topological phases characterized by $W = 0$, ± 1 and ± 2 for the different combinations of (h_1, h_2). For example, Fig. 9(c) depicts the topologically nontrivial phase with $W = +2$ for the set of hopping parameters $|h_1| = -1$ eV and $|h_2| = -0.8$ eV. On the other hand, choices of hopping parameters $|h_1| = -1$ eV and $|h_2| = -0.4$ eV render the state with $W = -2$. Moreover, for the completeness, we now consider two distinct hopping parameters for the intracell (h_{in}) and intercell (h_{out}) connections. And, for a fixed $h_{\text{in}}(= 1\,\text{eV}$, say), h_{out} is varied to obtain different phases as shown in Table III. Here, we have listed some of the particular cases; however, topological states are quite robust to the absolute values of the hopping parameters.

TABLE III. Different topological phases of the ribbon with different Zak phase and winding number.

Hopping parameters (eV)		Topological state	z	W
$(h_{\text{in}} = 1.0$	$h_{\text{out}} \leqslant 0.5)$	Trivial	0	0
$(h_{\text{in}} = 1.0$	$h_{\text{out}} = 0.7,\ 0.9)$	Nontrivial	$+\pi$	$+1$
$(h_{\text{in}} = 1.0$	$h_{\text{out}} = 1.0, 1.1)$	Nontrivial	$-\pi$	-1
$(h_{\text{in}} = 1.0$	$h_{\text{out}} = 1.2, 1.4)$	Nontrivial	$+2\pi$	$+2$
$(h_{\text{in}} = 1.0$	$h_{\text{out}} = 1.3)$	Nontrivial	-2π	-2

Therefore, we have observed that the 8-16-4 graphyne is one square symmetry lattice structure in which one can perform RSRG scheme systematically to obtain the *exact* analytical low-energy dispersion relation. Moreover, exact results match with the DFT outputs. In addition, this structure is purely carbon based; therefore, the effect of SOC is negligible as depicted in Fig. S6 of the Supplemental Material [80]. However, it exhibits edge states protected by nontrivial topological index, i.e., Zak phase or winding number. Therefore, this can be an important reference for investigating future topological phases made of light elements. Most importantly, this proposed structure indeed serves as an important missing link to other square symmetric Dirac lattices. In that sense, this structure is fascinating and possesses nontrivial morphological character compared to other existing structures.

IV. CONCLUSIONS

In summary, we have predicted a two-dimensional carbon allotrope, 8-16-4 graphyne with square symmetry from first-principles investigations. The structural stability of the system has been established by means of comprehensive investigation on the dynamic, thermal, and mechanical properties. In addition, the structural parameters of 8-16-4 graphyne are strongly supported by the crystal-structure prediction code USPEX. The presence of double-distorted Dirac nodal points along the symmetry path of the irreducible Brillouin zone is observed to be a dominant feature in its electronic band structure. This invariably indicates that 8-16-4 graphyne belongs to the family of 2D systems where square symmetry and Dirac nodal line semimetallic behavior coexist. In the presence of both inversion and time-reversal symmetry the Dirac loop forms around the symmetry points M for 8-16-4 graphyne. These nodal rings exhibit twofold band degeneracies at two distinct point of the symmetry path that disperse linearly. It refers to the fact that the hexagonal or rectangular symmetry is not a prerequisite for the existence of linear dispersion relation and that the VBM and CBM can meet each other at low-symmetry point also. In addition, we have availed an elegant approach in terms of RSRG scheme to analytically attain the generic dispersion relation for the class of square symmetric 2D Dirac nodal line semimetallic systems. Our exact analytical results are adequately supported by the DFT-based numerical outcomes. Nevertheless, this scheme essentially explores that the entire class of nodal line semimetals with square symmetry can be renormalized to an equivalent four-level system in the low-energy limit. This in turn validates the fascinating property regarding the universal feature of their band struc-

ture. Finally, the emergences of nontrivial topological aspects have been characterized by the nonvanishing Zak phase ($z = \pm\pi, \pm 2\pi$) in the presence of inversion and time-reversal symmetry. These results will assist in designing future materials and photonic crystals with nontrivial topological properties.

ACKNOWLEDGMENTS

A.B. sincerely acknowledges University Grants Commission (UGC), India for providing financial support through research fellowship. A.M. and R.A. would like to acknowledge the support from Carl Tryggers Stiftelse for Vetenskaplig Forskning (CTS), Olle Engkvists Stiftelse, and the Swedish Research Council (VR-2016-06014). SNIC and HPC2N are also acknowledged for providing computing time. S.C. would like to thank Skolkovo Institute of Science and Technology for providing computational resources.

APPENDIX: TRANSFORMATION EQUATIONS FROM Eq. (7) TO Eq. (9)

Equation (7) can be written as

$$\left\{(E-\varepsilon)-\frac{\left(t'^2+\lambda^2\right)}{(E-\varepsilon)}\right\}\varphi_e = t\varphi_a + \frac{t\lambda}{(E-\varepsilon)}\varphi_b + \frac{tt'}{(E-\varepsilon)}\varphi_d + \frac{2\lambda t'}{(E-\varepsilon)}\varphi_g.$$

Now, if we consider $E \approx \varepsilon$, In the left-hand side $(E-\varepsilon)$ can be neglected compared to $\frac{t'^2+\lambda^2}{(E-\varepsilon)}$. Then the above equation can be written as follows:

$$\left\{-\frac{\left(t'^2+\lambda^2\right)}{(E-\varepsilon)}\right\}\varphi_e = t\varphi_a + \frac{t\lambda}{(E-\varepsilon)}\varphi_b + \frac{tt'}{(E-\varepsilon)}\varphi_d + \frac{2\lambda t'}{(E-\varepsilon)}\varphi_g.$$

Or,

$$\varphi_e = -\frac{(E-\varepsilon)}{\left(t'^2+\lambda^2\right)}t\varphi_a - \frac{(E-\varepsilon)}{\left(t'^2+\lambda^2\right)}\frac{t\lambda}{(E-\varepsilon)}\varphi_b - \frac{(E-\varepsilon)}{\left(t'^2+\lambda^2\right)}\frac{tt'}{(E-\varepsilon)}\varphi_d - \frac{(E-\varepsilon)}{\left(t'^2+\lambda^2\right)}\frac{2\lambda t'}{(E-\varepsilon)}\varphi_g.$$

Or,

$$\varphi_e = -\frac{(E-\varepsilon)}{t'^2+\lambda^2}t\varphi_a - \frac{t\lambda}{t'^2+\lambda^2}\varphi_b - \frac{tt'}{t'^2+\lambda^2}\varphi_d - \frac{2\lambda t'}{t'^2+\lambda^2}\varphi_g.$$

It is evident that under the condition $E \approx \epsilon$ the above equation can be written as follows:

$$\varphi_e = -\frac{t\lambda}{t'^2+\lambda^2}\varphi_b - \frac{tt'}{t'^2+\lambda^2}\varphi_d - \frac{2\lambda t'}{t'^2+\lambda^2}\varphi_g.$$

Therefore, we have obtained Eq. (9) from Eq. (7).

[1] A. H. C. Neto, F. Guinea, N. M. R. Peres, K. S. Geim, and A. K. Novoselov, The electronic properties of graphene, Rev. Mod. Phys. **81**, 109 (2009).
[2] X.-L. Qi and S.-C. Zhang, Topological insulators and superconductors, Rev. Mod. Phys. **83**, 1057 (2011).
[3] A.V. Balatsky, I. Vekhter, and J. X. Zhu, Impurity-induced states in conventional and unconventional superconductors. Rev. Mod. Phys. **78**, 373 (2006).
[4] Y. Zhang, Y.-W. Tan, H. L. Stormer, and P. Kim, Experimental observation of the quantum Hall effect and Berry's phase in graphene, Nature (London) **438**, 201, (2005).
[5] K. S. Novoselov, Z. Jiang, Y. Zhang, S. V. Morozov, H. L. Stormer, U. Zeitler, J. C. Maan, G. S. Boebinger, P. Kim, and A. K. Geim, Room-temperature quantum Hall effect in graphene, Science **315**, 1379 (2007).
[6] Z. Song, Z. Wang, W. Shi, G. Li, C. Fang, and B. A. Bernevig, All Magic Angles in Twisted Bilayer Graphene are Topological, Phys. Rev. Lett. **123**, 036401 (2019).
[7] G. Van Miert and C. M. Smith, Dirac cones beyond the honeycomb lattice: A symmetry-based approach, Phys. Rev. B **93**, 035401 (2016).
[8] J. Wang, S. Deng, Z. Liu, and Z. Liu, The rare two-dimensional materials with Dirac cones, Natl. Sci. Rev. **2**, 22 (2015).
[9] Y. Hasegawa, R. Konno, H. Nakano, and M. Kohmoto, Zero modes of tight-binding electrons on the honeycomb lattice, Phys. Rev. B **74**, 033413 (2006).
[10] P. Nath, S. Chowdhury, D. Sanyal, and D. Jana, Ab-initio calculation of electronic and optical properties of nitrogen and boron doped graphene nanosheet, Carbon **73**, 275 (2014).
[11] S. Cahangirov, M. Topsakal, E. Akturk, H. Sahin, and S. Ciraci, Two- and One-Dimensional Honeycomb Structures of Silicon and Germanium, Phys. Rev. Lett., **102**, 236804 (2009).
[12] S. Chowdhury and D. Jana, A theoretical review on electronic, magnetic and optical properties of silicene. Rep. Prog. Phys., **79**, 126501 (2016).
[13] S. Chowdhury, A. Majumdar, and D. Jana, Electronic and optical properties of the supercell of 8-Pmmn borophene modified on doping by H, Li, Be, and C: A DFT approach. Appl. Phys. A **125**, 360 (2019).
[14] A. Majumdar, X. Yang, W. Luo, S. Chowdhury, and S. Chakraborty, High exothermic dissociation in van der Waals like hexagonal two dimensional nitrogene from first–principles molecular dynamics. Appl. Surf. Sci. **529**, 146552 (2020).
[15] D. Malko, C. Neiss, F. Vines, and A. Gorling, Competition for Graphene: Graphynes with Direction-Dependent Dirac Cones, Phys. Rev. Lett. **108**, 086804 (2012).
[16] Z. Wang, X. Zhou, X. Zhang, Q. Zhu, H. Dong, M. Zhao, and A. R. Oganov, Phagraphene: A low-energy graphene allotrope composed of 5–6–7 carbon rings with distorted Dirac cones, Nano Lett. **15**, 6182 (2015).
[17] H. Yin, X. Shi, C. He, M.-M. Canales, J. Li, C. J. Pickard, C. Tang, T. Ouyang, C. Zhang, and J. Zhong, Stone-Wales graphene: A two-dimensional carbon semimetal with magic stability, Phys. Rev. B **99**, 041405(R) (2019).
[18] L.-C. Xu, R.-Z. Wang, M.-S. Miao, X.-L. Wei, Y.-P. Chen, H. Yan, W.-M. Lau, L.-M. Liu, and Y.-M. Ma, Two dimensional

Dirac carbon allotropes from graphene, Nanoscale **6**, 1113 (2014).
[19] X. Chen, A. Bouhon, L. Li, F. M. Peeters, and B. Sanyal, PAI-graphene: A new topological semimetallic two-dimensional carbon allotrope with highly tunable anisotropic Dirac cones, Carbon **170**, 477 (2020).
[20] C. Su, H. Jiang, and J. Feng, Two-dimensional carbon allotrope with strong electronic anisotropy, Phys. Rev. B **87**, 075453 (2013).
[21] M. Zhao, W. Dong, and A. Wang, Two-dimensional carbon topological insulators superior to graphene, Sci. Rep. **3**, 3532 (2013).
[22] L. Li, X. Kong, and F. M. Peeters, New nanoporous graphyne monolayer as nodal line semimetal: Double Dirac points with an ultrahigh Fermi velocity, Carbon **141**, 712 (2019).
[23] X. Zhang, L. Wei, J. Tan, and M. Zhao, Prediction of an ultrasoft graphene allotrope with Dirac cones, Carbon **105**, 323 (2016).
[24] H. Huang, W. Duan, and Z. Liu, The existence/absence of Dirac cones in graphynes, New J. Phys. **15**, 023004 (2013).
[25] A. Bandyopadhyay, S. Datta, D. Jana, S. Nath, and M. Uddin, The topology and robustness of two Dirac cones in S-graphene: A tight binding approach, Sci. Rep. **10**, 2502 (2020).
[26] J. Wang, H. Huang, W. Duan, and Z. Liu, Identifying Dirac cones in carbon allotropes with square symmetry, J. Chem. Phys., **139**, 184701 (2013).
[27] Z. Liu and J. Wang, and J. Li, Dirac cones in two-dimensional systems: From hexagonal to square lattices, Phys. Chem. Chem. Phys. **15**, 18855 (2013).
[28] A. Bandyopadhyay and D. Jana, A review on role of tetra-rings in graphene systems and their possible applications, Rep. Prog. Phys. **83**, 056501 (2020).
[29] S. Jana, A. Bandyopadhyay, and D. Jana, Acetylenic linkage dependent electronic and optical behaviour of morphologically distinct '-ynes', Phys. Chem. Chem. Phys. **21**, 13795 (2019).
[30] L. Z. Zhang, Z. F. Wang, Z. M. Wang, S. X. Du, H.-J. Gao, and F. Liu, Highly anisotropic Dirac fermions in square graphynes, J. Phys. Chem. Lett. **6**, 2959 (2015).
[31] S.-Y. Yang, H. Yang, E. Derunova, S. S. P. Parkin, B. Yan, and M. N. Ali, Symmetry demanded topological nodal-line materials, Adv. Phys: X, **3**, 1414631 (2018).
[32] W. Jiang, M. Kang, H. Huang, H. Xu, T. Low, and F. Liu, Topological band evolution between Lieb and Kagome lattices. Phys. Rev. B **99**, 125131 (2019).
[33] W. Jiang, S. Zhang, Z. Wang, F. Liu, and T. Low. Topological band engineering of Lieb lattice in phthalocyanine-based metal-organic frameworks, Nano. Lett. **20**, 1959 (2020).
[34] H. Wu, Y. Qian, Z. Du, R. Zhu, E. Kan, and K. Deng, Prediction of another semimetallic silicene allotrope with Dirac fermions, Phys. Lett. A, **381**, 3754 (2017).
[35] C. Xu, Y. Wang, R. Han, H. Tu, and Y Yan, Topological node line semimetal state in two-dimensional tetragonal allotrope of Ge and Sn, New J. Phys. **21**, 033005 (2019).
[36] D. Sticlet, F. Piéchon, J.-N. Fuchs, P. Kalugin, and P. Simon, Geometrical engineering of a two band Chern insulator in two dimensions with arbitrary topological index, Phys. Rev. B **85**, 165456 (2012).
[37] A. Yamakage, K.-I. Imura, J. Cayssol, and Y. Kuramoto, Interfacial charge and spin transport in Z_2 topological insulators, Phys. Rev. B **83**, 125401 (2011).
[38] J. T. Wang, S. Nie, H. Weng, Y. Kawazoe, and C. Chen, Topological Nodal-Net Semimetal in a Graphene Network Structure, Phys. Rev. Lett. **120**, 026402 (2018).
[39] Y. Gao, W. Wu, P.-J. Guo, C. Zhong, S. A. Yang, K. Liu, and Z.-Y. Lu, Hexagonal supertetrahedral boron: A topological metal with multiple spin-orbit-free emergent fermions, Phys. Rev. Mater. **3**, 044202 (2019).
[40] A. A. Zyuzin and A. A. Burkov, Topological response in Weyl semimetals and the chiral anomaly, Phys. Rev. B **86**, 115133 (2012).
[41] B. A. Bernevig and T. L. Hughes, *Topological Insulators and Topological Superconductors* (Princeton University Press, Princeton, NJ, 2013).
[42] Y. Chen, Y. Xie, X. Yan, M. L. Cohen, and S. Zhang, Topological carbon materials: A new perspective, Phys. Rep. **868**, 1 (2020).
[43] B. W. Southern, A. A. Kumar, and J. A. Ashraff, Real-space rescaling method for disordered systems, Phys. Rev. B **28**, 1785 (1983).
[44] X.-D. Chen, W. M. Deng, F.-L. Shi, F.-L. Zhao, M. Chen, and J.-W. Dong, Direct Observation of Corner States in Second-Order Topological Photonic Crystal Slabs, Phys. Rev. Lett. **122**, 233902 (2019).
[45] M. Xiao, Z. Q. Zhang, and C. T. Chan, Surface Impedance and Bulk Band Geometric Phases in One-Dimensional Systems, Phys. Rev. X **4**, 021017 (2014).
[46] Y. Liu, C.-S. Lian, Y. Li, Y. Xu, and W. Duan, Pseudospins and Topological Effects of Phonons in a Kekulé Lattice, Phys. Rev. Lett. **119**, 255901 (2017).
[47] Z. Zhang, M. R. Lopage, Y. Cheng, X. Liu, and J. Christensen, Non-Hermitian Sonic Second-Order Topological Insulator, Phys. Rev. Lett. **122**, 195501 (2019).
[48] P. Hohenberg and W. Kohn, Inhomogeneous electron gas, Phys. Rev. **136**, B864 (1964).
[49] W. Kohn and L. J. Sham, Self-consistent equations including exchange and correlation effects, Phys. Rev. **140**, A1133 (1965).
[50] P. E. Blochl, Projector augmented-wave method, Phys. Rev. B **50**, 17953 (1994).
[51] G. Kresse and J. Furthmüller, Efficient iterative schemes for *ab initio* total-energy calculations using a plane-wave basis set, Phys. Rev. B - Condens. Matter Mater. Phys. **54**, 11169 (1996).
[52] H. J. Monkhorst and J. D. Pack, Special points for Brillouin-zone integrations, Phys. Rev. B, **13**, 5188 (1976).
[53] J. P. Perdew, K. Burke, and M. Ernzerhof, Generalized Gradient Approximation Made Simple, Phys. Rev. Lett. **77**, 3865 (1996).
[54] A. Togo and I. Tanaka, First principles phonon calculations in materials science, Scr. Mater. **108**, 1 (2015).
[55] S. Nosé, A unified formulation of the constant temperature molecular dynamics methods, J. Chem. Phys. **81**, 511 (1984).
[56] Q. Wu, S. Zhang, H. Song, M. Troyer, and A. A. Soluyanov, WannierTools: An open-source software package for novel topological materials, Comput. Phys. Commun. **224**, 405 (2018).
[57] A. A. Mostofi, J. R. Yates, G. Pizzi, Y. Lee, I. Souza, D. Vanderbilt, and N. Marzari, An updated version of WANNIER90: A tool for obtaining maximally-localised Wannier functions, Comput. Phys. Commun. **185**, 2309 (2014).

[58] S. Maintz, V. L. Deringer, A. L. Tchougreeff, and R. Dronskowski, LOBSTER: A tool to extract chemical bonding from plane-wave based DFT, J. Comput. Chem. **37**, 1030 (2016).

[59] C. W. Glass, A. R. Oganov, and N. Hansen, USPEX—Evolutionary crystal structure prediction, Comput. Phys. Commun. **175**, 713 (2006).

[60] A. R. Oganov and C. W. Glass, Crystal structure prediction using ab initio evolutionary techniques: Principles and applications, J. Chem. Phys. **124**, 244704 (2006).

[61] Q. Zhu, L. Li, A. R. Oganov, and P. B. Allen, Evolutionary method for predicting surface reconstructions with variable stoichiometry, Phys. Rev. B **87**, 195317 (2013).

[62] X. Yang, Z. Dai, Y. Zhao, and S. Meng, Phonon thermal transport in a class of graphene allotropes from first principles, Phys. Chem. Chem. Phys **20**, 15980 (2018).

[63] B. Peng, H. Zhang, H. Shao, Y. Xu, G. Ni, R. Zhang, and H. Zhu, Phonon transport properties of two-dimensional group-IV materials from ab initio calculations, Phys. Rev. B **94**, 245420 (2016).

[64] B. Peng, H. Zhang, H. Shao, Y. Xu, R. Zhang, H. Lu, D. W. Zhang, and H. Zhu, First-principles prediction of ultralow lattice thermal conductivity of dumbbell silicene: A comparison with low-buckled silicene, ACS Appl. Mater. Interfaces **8**, 20977 (2016).

[65] M. Born, On the stability of crystal lattices, Math. Proc. Cambridge Philos. Soc. **36**, 160 (1940).

[66] D. Akinwande, C. J. Brennan, J. S. Bunch, P. Egberts, J. R. Felts, H. Gao, R. Huang, J. Kim, T. Li, Y. Li, K. M. Liechti, N. Lu, H. S. Park, E. J. Reed, P. Wang, B. I. Yakobson, T. Zhang, Y. Zhang, Y. Zhou, and Y. Zhu, A review on mechanics and mechanical properties of 2D materials—Graphene and beyond, Extreme Mech. Lett. **13**, 42 (2017).

[67] K. N. Kudin, G. E. Scuseria, and B. I. Yakobson, C_2F, BN, and C nanoshell elasticity from ab initio computations, Phys. Rev. B **64**, 235406 (2001).

[68] S. W. Cranford and M. J. Buehler, Mechanical properties of graphyne, Carbon **49**, 4111 (2011).

[69] K. Cocq, N. Saffon-Merceron, Y. Coppel, C. Poidevin, V. Maraval, and R. Chauvin, carbo-Naphthalene: A polycyclic carbo-benzenoid fragment of α-graphyne, Angew. Chemie - Int. Ed. **55**, 15133 (2016).

[70] W.-X. Zhou and K.-Q. Chen, Enhancement of thermoelectric performance in β-graphyne nanoribbons by suppressing phononic thermal conductance, Carbon **85**, 24 (2015).

[71] S. C. Shekar and R. S. Swati, Molecular switching on graphyne and graphdiyne: Realizing functional carbon networks in synergy with graphene, Carbon, **126**, 489 (2018).

[72] J. M. Kehoe, J. H. Kiley, J. J. English, C. A. Johnson, R. C. Petersen, and M. M. Haley, Carbon networks based on Dehydrobenzoannulenes. 3. Synthesis of graphyne substructures, Org. Lett. **2**, 969 (2000).

[73] B. Kang and J. Y. Lee, Electronic properties of α-graphyne nanotubes, Carbon **84**, 246 (2015).

[74] M. Gholami, F. Melin, R. Mcdonald, M. J. Ferguson, L. Echegoyen, and R. R. Tykwinski, Synthesis and characterization of expanded radialenes, bisradialenes, and radiaannulenes, Angew. Chemie - Int. Ed. **46**, 9081 (2007).

[75] B. Dong, H. Guo, Z. Liu, T. Yang, P. Tao, S. Tang, R. Saito, and Z. Zhang, Spontaneous antiferromagnetic order and strain effect on electronic properties of α-graphyne, Carbon, **131**, 223 (2018).

[76] F. Diederich and M. Kivala, All-carbon scaffolds by rational design, Adv. Mater. **22**, 803 (2010).

[77] H. Huang, Y. Li, Z. Liu, J. Wu, and W. Duan, Comment on "Structural and Electronic Properties of T Graphene: A Two-Dimensional Carbon Allotrope with Tetrarings," Phys. Rev. Lett. **110**, 029603 (2013).

[78] S. Sil, S. N. Karmakar, R. K. Moitra, and A. Chakrabarti, Extended states in one-dimensional lattices: Application to the quasiperiodic copper-mean chain, Phys. Rev. B **48**, 4192 (1993); see also A. Mukherjee, A. Nandy, S. Sil, and A. Chakrabarti, Engineering topological phase transition and Aharonov–Bohm caging in a flux-staggered lattice, J. Phys.: Condens. Matter **33**, 035502 (2021).

[79] B. G. Kim and H. J. Choi, Graphyne: Hexagonal network of carbon with versatile Dirac cones, Phys. Rev. B **86**, 115435 (2012).

[80] See Supplemental Material at http://link.aps.org/supplemental/10.1103/PhysRevB.103.075137 for the details of the fate of Dirac points between different symmetry points, comparison of Fermi velocity with other 2D carbon allotropes, other possible band structure from the universal dispersion relation, and band structure of the nanoribbon.

[81] J. Zak, Berry's Phase for Energy Bands in Solids, Phys. Rev. Lett. **62**, 2747 (1989).

[82] F. Liu and K. Wakabayashi, Novel Topological Phase with a Zero Berry Curvature, Phys. Rev. Lett. **118**, 076803 (2017).

[83] B. Y. Xie, G. X. Su, H. F. Wang, H. Su, X. P. Shen, P. Zhan, M. H. Lu, Z. L. Wang, and Y. F. Chen, Visualization of Higher-Order Topological Insulating Phases in Two-Dimensional Dielectric Photonic Crystals, Phys. Rev. Lett. **122**, 233903 (2019).

[84] W. P. Su, J. R. Schrieffer, and A. Heeger, Solitons in Polyacetylene, Phys. Rev. Lett. **42**, 1698 (1979).

[85] D. Obana, F. Liu, and K. Wakabayashi, Topological edge states in the Su-Schrieffer-Heeger model, Phys. Rev. B **100**, 075437 (2019).